Understanding of Enhanced Oxygen Storage Capacity in $Ce_{0.5}Zr_{0.5}O_2$: The Presence of an Anharmonic Pair Distribution Function in the $Zr-O_2$ Subshell as Analyzed by XAFS Spectroscopy

S. Lemaux, A. Bensaddik, A. M. J. van der Eerden, J. H. Bitter,* and D. C. Koningsberger

Department of Inorganic Chemistry and Catalysis, Debye Institute, Utrecht University, P.O. Box 80083, 3508 TB Utrecht, The Netherlands

Received: August 29, 2000; In Final Form: March 13, 2001

Standard EXAFS analysis on $Ce_xZr_{1-x}O_2$ mixed oxides leads to incorrect structural parameters. A comparison of XRD Rietveld analysis with an EXAFS study of a Y-doped reference compound and a $Ce_{0.5}Zr_{0.5}O_2$ catalyst showed that in order to obtain reliable structural parameters with EXAFS an anharmonic pair distribution function has to be used for the analysis of the second Zr−O bond. The anharmonicity of the second Zr−O subshell points to a much weaker Zr−O bond than in the first Zr−O subshell. A lamellar type structural model explains the high oxygen storage capacity of $Ce_{0.5}Zr_{0.5}O_2$. The short $Zr-O_1$ distance corresponds to the *intra*layer Zr−O bond and the much weaker $Zr-O_2$ distance to the *inter*layer Zr−O interaction. The oxygen storage capacity is determined by the *inter*layer Zr−O interaction.

Introduction

$Zr_xCe_{1-x}O_2$ mixed oxides have been extensively studied since they are good candidates for noble metal (Pd, Pt, or Rh) support in automotive three way catalysts (TWCs). Compared to pure Ce-oxide they present an enhancement of the oxygen storage/release capacity (OSC), a crucial property for three-way catalysts.[1] This property is very important because it allows the catalyst to operate in an enlarged air-to-fuel window. Several studies indicate that the OSC of ZrO_2 based materials are closely related to their structure.[2,3] It is therefore indispensable to unambiguously determine their structural properties.

Because of the ability of the EXAFS technique to probe the local structure around the Zr absorber atom, EXAFS has been extensively used to study several ZrO_2 based materials.[2−7] For $Ce_{0.5}Zr_{0.5}O_2$, eight oxygen atoms around a central Zr atom are expected[8] (two shells of four atoms for a tetragonal structure or one shell of eight atoms for a cubic structure). As already pointed out by Yashima,[9] the method used for the EXAFS analysis can drastically affect the obtained results. In particular, in some recent XAFS studies,[2,3] less than the expected 8 oxygen atoms were determined using a Zr K edge EXAFS analysis method in which the data were fitted with a 4+2 shell distribution (four oxygen atoms at 2.115 Å and two oxygen atoms at 2.324 Å). In that study the inner potential (E_0) values of the two Zr−O subshells were preset to be equal during the EXAFS analysis. These authors claim that the OSC is due to a softening of the bonding of some of the oxygens in the second shell and that the missing oxygen oxygen atoms become very delocalized in the lattice.

In this paper the structure of $Ce_{0.5}Zr_{0.5}O_2$ is further investigated by combining the results of XRD and XAFS spectroscopy. First, a well-defined tetragonal $Y-ZrO_2$ sample (1 mol % $Y_2O_3-ZrO_2$) with two subshells of four oxygen atoms around Zr is used as model compound. The refinement of the cell parameters of this sample is based on their powder XRD pattern. The comparison of both the XRD and the EXAFS results shows that the assumption of equal E_0 values for both Zr−O subshells in $Y-ZrO_2$ leads to wrong coordination numbers. However, leaving the E_0 values free in the EXAFS fitting procedure resulted in a lower coordination distance of the second subshell than obtained with XRD. It will be shown that the anharmonic behavior of the pair distribution function of the second Zr−O subshell is the origin of the discrepancy between the EXAFS and the XRD results. A good agreement between XRD and EXAFS results is obtained by using a cumulant expansion approach for the EXAFS analysis of the second Zr−O subshell. Applying the same data-analysis method in the study of the structure of $Ce_{0.5}Zr_{0.5}O_2$ similar results are obtained. The anharmonicity of the pair distribution function is much larger for $Ce_{0.5}Zr_{0.5}O_2$. The higher anharmonicity of the $Zr-O_2$ subshell can be related to the enhanced oxygen storage capacity of $Ce_{0.5}Zr_{0.5}O_2$.

Experimental Section

The 1 mol % $Y_2O_3-ZrO_2$ compound was obtained from Gimex (grain size between 0.5 μm and 1 μm), the $Ce_{0.5}Zr_{0.5}O_2$ was a high surface area (106 m^2/g) CEZIRENCAT sample[11] and purchased from Rhodia.

XRD was performed on an INEL PDS 120 powder diffractometer system (filtered Co $K\alpha_1$ radiation). The powder pattern analysis were processed by using the Rietveld analysis method with the program GSAS.[12]

The XAFS data were measured at the ESRF (beamline BM29) at room temperature using a Si (111) double-crystal monochromator. The higher harmonics were removed by detuning the monochromator to 50%. The energies of the spectrum were calibrated by simultaneously measuring the spectra of the sample and of a Zr foil.

Standard procedures were used to extract the EXAFS signal by using the XDAP program.[13] The preedge background was approximated by a modified Victoreen curve.[14] Normalization was done by dividing the height of the absorption edge at 50

* Corresponding author.

10.1021/jp003111t CCC: $20.00
Published on Web 05/04/2001

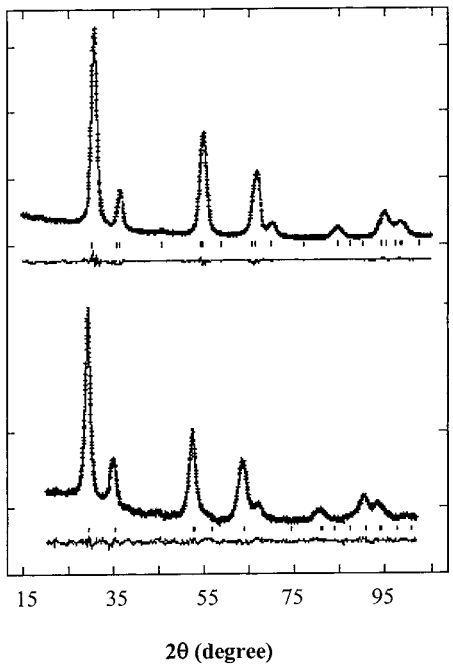

Figure 1. Comparison of the calculated XRD patterns (crosses) by the Rietveld analysis with the experimental patterns (line). Their differences are plotted on the same scale. Top pattern: 1 mol % $Y_2O_3-ZrO_2$. Bottom pattern: $Ce_{0.5}Zr_{0.5}O_2$.

TABLE 1: Structural Parameters of the 1 mol % Y_2O_3 ZrO_2 and of $Ce_{0.5}Zr_{0.5}O_2$ Samples Determined by Rietveld Method Analysis

	1 mol %Y_2O_3. ZrO_2 (space group: $P4_2/nmc$)	$Ce_{0.5}Zr_{0.5}O_2$ (space group: $P4_2/nmc$)
a (Å)	3.5931(2)	3.724(3)
c (Å)	5.166(2)	5.296(8)
$c/(a\sqrt{2})$	1.017	1.006
cation x	0.75	0.75
cation y	0.25	0.25
cation z	0.25	0.25
O x	0.25	0.25
O y	0.25	0.25
O z	0.4591(8)	0.461(4)
R_{wp} (%)	3.2	1.8
χ^2	7.6	1.8
d Zr−O_I (Å)	2.096	2.168
d Zr −O_{II} (Å)	2.343	2.410

eV. Multishell fittings were performed in the R space by minimizing the difference between the imaginary part and the magnitude of the Fourier transform of the raw data and the model EXAFS function. The advantages of fitting in R space are extensively discussed elsewhere.[15,16] The difference file technique was used to determine more reliably the individual contributions of the two Zr−O subshells in the first shell region of the Fourier transform.[15]

Results

XRD. CeO_2 powder was used as an internal standard for calibration of the diffractometer to establish precisely the values of the cell parameters. The XRD patterns of both the 1 mol % $Y_2O_3-ZrO_2$ and $Ce_{0.5}Zr_{0.5}O_2$ sample were indexed in the $P4_2/nmc$ space group with a quadratic unit cell (Table 1). The quality of the Rietveld analysis can be seen in Figure 1. The use of Rietveld analysis for refinement of the position of the oxygen atoms lead to atomic positions characteristic of tetragonal ZrO_2.[17] This oxide possesses two oxygen coordination shells around Zr with 4 oxygen neighbors each. The isotropic atomic thermal parameters B are not listed because the absorption correction could not be performed accurately.

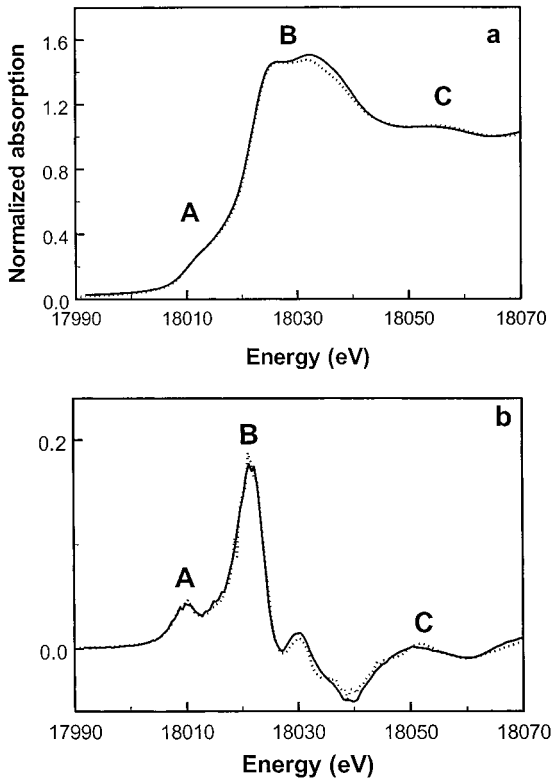

Figure 2. (a) Zr K edge XANES spectra of 1 mol % $Y_2O_3-ZrO_2$ (solid line) and $Ce_{0.5}Zr_{0.5}O_2$ (dotted line). (b) First derivatives of these spectra.

XANES. Figure 2 shows the Zr K edge XANES spectra and the first derivatives of the XANES data of the 1 mol % $Y_2O_3-ZrO_2$ and $Ce_{0.5}Zr_{0.5}O_2$ samples. The XANES spectral region can be divided in three parts (denoted as A, B, and C) as shown previously.[7] The origin of energy, i.e., E_0, was taken at the inflection point of the rising edge after the A structure. For comparison of the XANES spectra, normalization was done at 18066 eV. Figure 2 shows clearly that the three features are very similar for both 1 mol % $Y_2O_3-ZrO_2$ and $Ce_{0.5}Zr_{0.5}O_2$. In particular, the preedge features A, characteristic of a tetragonal structure,[7] are the same for both two samples.

EXAFS. The raw EXAFS data of the 1 mol % $Y_2O_3-ZrO_2$ and the $Ce_{0.5}Zr_{0.5}O_2$ samples are shown in Figure 3a. It can be seen that the data quality is excellent (S/N ratio is 50 at $k = 3$ Å^{-1} and 8 at $k = 15$ Å^{-1}) for the $Y_2O_3-ZrO_2$ standard sample. The corresponding Fourier transforms (k^2, $2.5 < k < 15$ Å^{-1}) are plotted in Figure 3b. The first shell region ($0 < R < 2.5$ Å) is similar for both samples; small but significant changes can be observed for ($1.8 < R < 2.5$ Å) in both the magnitude and the imaginary part of the Fourier transforms.

For each of the two Zr−O subshells in the $Y_2O_3-ZrO_2$ sample, separate phase and backscattering amplitude functions were calculated with the FEFF7 program. The coordination number and distance as derived from our XRD results of the Y-doped sample were used as fixed input values for this calculation. For each subshell the amplitude reduction factor (S_o^2) was chosen to be 1 with the lifetime broadening (V_i) equal to 0 eV. Next, the values for the inner potential shift (V_r) and the disorder (σ^2) for each subshell were optimized in the FEFF7 calculation to find a zero value for the difference in innerpotential value (ΔE_0) and disorder ($\Delta\sigma^2$) in the fit of the two Zr−O subshells of the 1 mol % $Y_2O_3-ZrO_2$ sample. The multiple-

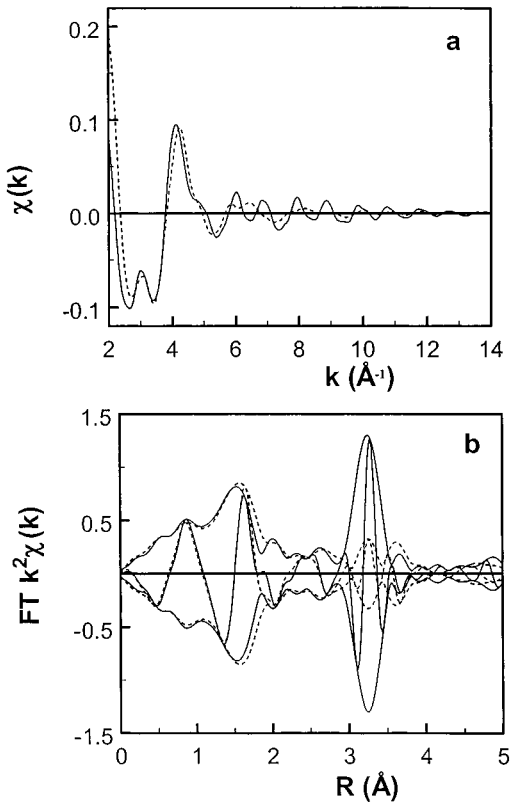

Figure 3. (a) Raw EXAFS data of 1 mol % (solid line) and $Ce_{0.5}Zr_{0.5}O_2$ (dotted line). b) Corresponding Fourier transforms (k^2, 2.5 < k <15 Å^{-1}).

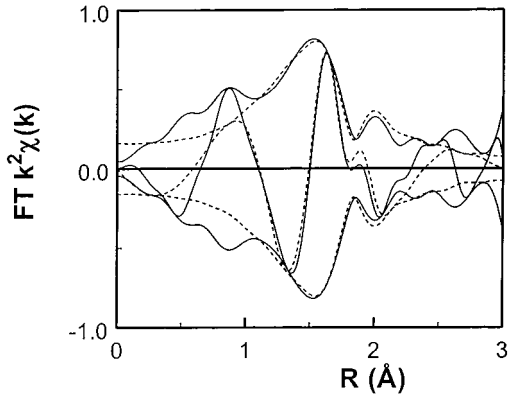

Figure 4. R-space fit (dotted line) (k^2, 2.5 < k <15 Å^{-1}, 1 < R <2.3 Å, with free parameters: $\Delta\sigma^2$ and ΔE_0) of EXAFS data (solid line) of 1 mol % $Y_2O_3-ZrO_2$ using FEFF7 phase shifts and backscattering amplitudes calculated with the input parameters as given in Table 2.

shell fit was performed in the R space between 1 and 2.3 Å (no phase correction and a k^2 weighting) using a k range 2.5 < k < 15 Å^{-1}. The fit results are given in Figure 4 with a dotted line. The variances of the fit for the absolute value (V_{abs}) and imaginary part (V_{im}) of the Fourier transform are given in Table 2 together with the final FEFF7 input parameters. The FEFF7 input values of V_r and σ^2 for the Zr−O_2 subshell are 4.7 eV and 10×10^{-3} Å^2 higher than for the Zr−O_1 subshell, showing a different type of oxygen coordination with a larger disorder for the Zr−O_2 subshell. The calibrated Zr−O_1 and Zr−O_2 phase shift and backscattering amplitude functions were now used in three different methods of the EXAFS analysis of the 1 mol % $Y_2O_3-ZrO_2$ and $Ce_{0.5}Zr_{0.5}O_2$ samples.

In method I, a refinement of the EXAFS parameters was performed by fitting in addition to the innerpotential value (ΔE_0)

TABLE 2: Zr K Edge EXAFS Parameters of 1 mol % $Y_2O_3-ZrO_2$ by Using FEFF7[a] Zr−O_1 and Zr−O_2 Phase Shifts and Backscattering Amplitudes

N	R (Å)	$\Delta\sigma^b$ (10^3 Å^2)	ΔE_0 (eV)	V_{im}[c]	V_{abs}[c]
4[b]	2.096[b]	0	0	3.8	0.5
4[b]	2.343[b]	0	0		

[a] FEFF7 input: $V_i = 0$, $S_0^2 = 1$. For Zr−O_1: $N = 4$, $R = 2.096$ Å, $\sigma^2 = 5 \times 10^{-3}$ Å^2, $V_r = -5.1$ eV. For Zr−O_2: $N = 4$, $R = 2.343$ Å, $\sigma^2 = 14.5 \times 10^{-3}$ Å^2, $V_r = -0.8$ eV. [b] XRD values, fixed in analysis. [c] Fit variance in percent.

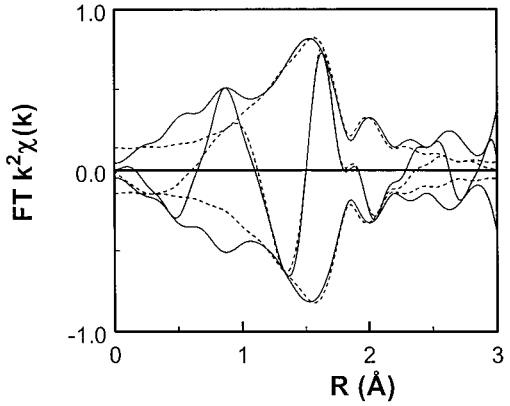

Figure 5. Method I: R-space fit (dotted line) (k^2, 2.5 < k <15 Å^{-1}, 1 < R <2.3 Å, with free parameters: $\Delta\sigma^2$, ΔE_0, and R) of EXAFS data (solid line) of 1 mol % $Y_2O_3-ZrO_2$ using FEFF7 phase shifts and backscattering amplitudes calculated with the input parameters as given in Table 2.

and disorder ($\Delta\sigma^2$) also the coordination distances of the two Zr−O subshells. The FEFF7 Zr−O_1 and the Zr−O_2 phase shift and backscattering amplitude obtained with the method described above were used in the fit procedure. For the 1 mol % $Y_2O_3-ZrO_2$ sample a lower variance of the fit of the imaginary part (V_{im}) of the Fourier transform was obtained with a significant lower Zr−O_2 coordination distance (2.27 vs 2.34 Å) (see Tables 2 and 3), implying a discrepancy between the EXAFS and the XRD results. The differences between the R space fit using method I and the R space fit obtained in calibrating the FEFF7 references with fixing the Zr−O_1 and Zr−O distances to the XRD values can be observed by comparing Figure 4 with Figure 5. In Figure 5 the Fourier transformed EXAFS data and the fit using method I (free R, $\Delta\sigma^2$, and ΔE_0) are compiled. By using method I a better agreement between the imaginary parts of the Fourier transform and the fit is obtained especially in the region 1.8 < R < 2.3 Å.

The difference file technique was used to check the fit quality of both subshells. The agreement between the Fourier transform of the difference file and the calculated fitted contribution in the R range used for the R space fit can be judged in Figure 6. Figure 6a gives the Fourier transform (k^2, 2.5 < k < 15 Å^{-1}) of the difference file (solid line: raw EXAFS minus Zr−O_2) and the fitted Zr−O_1 contribution (dotted line). The Fourier transforms of the difference file (solid line: raw EXAFS minus Zr−O_1) and the fitted Zr−O_2 contribution (dotted line) are shown in Figure 6b. The calculated fitted Zr−O_1 and Zr−O_2 EXAFS functions (k^2 weighted) using method I are plotted in Figure 6c (thin lines). This figure demonstrates the anti-phase behavior of both Zr−O subshells.

To compare these results with the literature, the same Zr−O phase shift and backscattering amplitude was used for the analysis of both Zr−O subshells. The set that was calibrated to

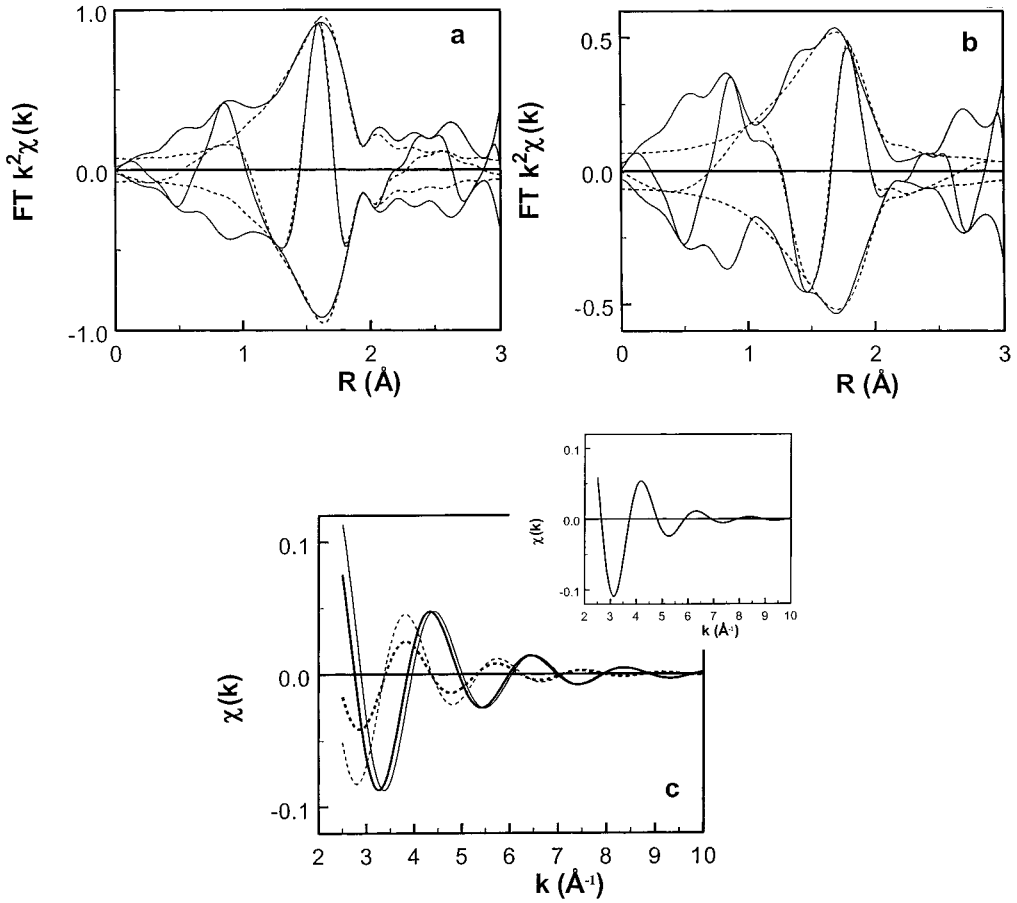

Figure 6. (a) Fourier transform ((k^2, 2.5 < k < 15 Å^{-1}) of Zr−O_1 difference file (raw data minus Zr−O_2) (solid line) and fitted Zr−O_1 contribution (dotted line), (b) Fourier transform ((k^2, 2.5 < k <15 Å^{-1}) of Zr−O_2 difference file (Raw data minus Zr−O_1) (solid line) and fitted Zr−O_2 contribution (dotted line), (c) EXAFS functions of fitted Zr−O_1 using model I (thin solid line) and Zr−O_2 contributions using model I (thin dotted line). EXAFS functions of fitted Zr−O_1 using model II (thick solid line) and Zr−O_2 contributions using model II (thick dotted line). Both models lead to the same total Chi function (inset).

the Zr−O_1 subshell was used as a reference. First, in method II, the analysis described by Vlaic et al.[2,3] was applied: the inner potential (ΔE_0) is allowed to float in the fitting procedure, but set to the same value for both the two shells. The coordination numbers were fixed with a 4+2 shell distribution (four oxygen atoms at a short and two oxygen atoms at a longer coordination distance), using the structural model as put forward by Vlaic et al.[2,3] The variances V_{im} and V_{abs} of the fit are similar as obtained with fit procedure described above (Table 3). The coordination distance of the Zr−O_2 subshell is now closer (2.29 vs 2.34 Å) to the XRD value and the disorder obtained for both Zr−O subshells is similar. Figure 6c (thick lines) explains the discrepancy between the results of Vlaic et al.[2,3] and the results obtained in this work. The sum of the Zr−O_1 and Zr−O_2 contribution is in both cases the same (inset Figure 6c), which explains the similar variances of V_{im} and V_{abs} obtained with both methods. However, by forcing the inner potential to be the same a wrong coordination number for the second shell is obtained. The combination of a wrong ΔE_0 for both shells with a wrong coordination number of the second shell can still lead to the same total sum.

In method III a 4+4 shell distribution was applied with the ΔE_0 values free to vary during the fit procedure. Also in this case the FEFF7 Zr−O_1 phase shift and backscattering amplitude was used for analyzing both Zr−O subshells. No improvement of the R-space fit was obtained (Table 3). The coordination distance of the Zr−O_2 subshell is 0.07 Å smaller than the value found by our XRD analysis, a similar result as obtained with method I and the Debye−Waller of the second oxygen subshell is 6×10^{-3} higher than for Zr−O_1.

The EXAFS analysis of the $Ce_{0.5}Zr_{0.5}O_2$ sample was carried out using the same three methods. Similar results were obtained as with 1 mol % Y_2O_3−ZrO_2. However, the apparent contraction of the second Zr−O subshell appears to be 0.17 Å, about 0.1 Å larger as detected for the Y_2O_3−ZrO_2 standard sample.

Finally the cumulant expansion approach was used for EXAFS analysis of the second oxygen shell by adding to the FEFF7 phase shift a term: $-4/3C_3k$.[3,18,19] It was indeed possible to obtain the same coordination distance as detected in 1 mol % Y_2O_3−ZrO_2 with XRD by adjusting the anharmonicity parameter C_3. The results are given in Table 4. The inner potential values found for the Zr−O_2 subshells are now similar as found for the Zr−O_1 subshells. Moreover, the disorder and the anharmonicity of the Zr−O_2 subshell in $Ce_{0.5}Zr_{0.5}O_2$ are larger than for the corresponding subshell of the Y_2O_3−ZrO_2 standard sample.

Discussion

XRD and XAFS. The XRD patterns of both Y−Zr and Ce−Zr oxides can be indexed in the $P4_2/nmc$ space group with a quadratic unit cell. Our XRD analysis on 1 mol % Y_2O_3−ZrO_2 confirmed the previously published XRD[7] unit cell parameters: a = 3.5931(2) Å and c = 5.166(2) Å. It is known that this oxide possesses two oxygen coordination shells around Zr with 4 oxygen neighbors each. The Rietveld analysis carried

TABLE 3: Zr K-edge EXAFS Analysis Parameters of 1 mol % $Y_2O_3-ZrO_2$ and $Ce_{0.5}Zr_{0.5}O_2$

	1 mol % Y_2O_3. ZrO_2					$Ce_{0.5}Zr_{0.5}O_2$				
method	N	R (Å)	$\Delta\sigma^2$ (10^3 Å^2)	ΔE_0 (eV)	V_{im} V_{abs}	N	R (Å)	$\Delta\sigma^2$ (10^3 Å^2)	ΔE_0 (eV)	V_{im} V_{abs}
I	4[a]	2.101	−0.8	−1.4	0.963	4[a]	2.114	0	−3.6	1.54
	4[a]	2.272	−4.7	5.9	0.364	4[a]	2.238	−6.6	7.1	0.428
II	4[a]	2.099	−0.5	1.5[?]	0.958	4[a]	2.119	0	−0.5[b]	1.84
	2[a]	2.293	0.7	1.5[?]	0.508	2[a]	2.276	1.6	−0.5[b]	0.419
III	4[a]	2.099	−0.7	−1.1	0.921	4[a]	2.112	0.0	−3.4	1.55
	4[a]	2.267	5.1	3.6	0.407	4[a]	2.233	3.0	4.7	0.494

[a] Fixed in analysis. [b] Free but both equal.

TABLE 4: Zr K Edge EXAFS Analysis Parameters of the Second Oxygen Shell of 1 mol % $Y_2O_3-ZrO_2$ and $Ce_{0.5}Zr_{0.5}O_2$ Using the Cumulant Expansion Approach

	1 mol % Y_2O_3. ZrO_2						$Ce_{0.5}Zr_{0.5}O_2$					
N	R (Å)	σ^2 (10^3 Å^2)	ΔE_0 (eV)	C_3	V_{im}	V_{abs}	N	R (Å)	σ^2 (10^3 Å^2)	ΔE_0 (eV)	C_3	V_{im}	V_{abs}
4[a]	2.343	5.1	0.2	3.5×10^{-3}	1.4	0.4	4[a]	2.36	7.4	−3.0	5×10^{-3}	3.9	1.4

[a] Fixed in analysis.

out for both oxides in this study is fully in agreement with this structure.

Figure 2 shows clearly that the three XANES features (A, B, and C) are very similar for both 1 mol % $Y_2O_3-ZrO_2$ and $Ce_{0.5}Zr_{0.5}O_2$. In particular, the preedge feature A, characteristic of a tetragonal structure,[7] is the same for both two samples. Moreover, the first shell region of the Fourier transform of the raw EXAFS data of both oxides (see Figure 3b) is almost identical. Additionally, the EXAFS data-analysis using methods I, II ,and III applied to the $Ce_{0.5}Zr_{0.5}O_2$ sample show the same trends as found for the standard $Y_2O_3-ZrO_2$. By combining the XRD and the XAFS data it can be concluded that both samples have a similar 4+4 geometry in the two Zr−O subshells.

Therefore, EXAFS data analysis method II, which leads to a 4+2 model is wrong and must be rejected. In these data-analysis method put forward by Vlaic et al. the inner potential was preset to be equal. The $Zr-O_1$ and $Zr-O_2$ EXAFS functions as plotted in Figure 6c using method I (thin lines) show a strong antiphase behavior. Figure 6c explains why a false coordination number is obtained when the inner potential values are preset to be equal: the influence of a wrongly chosen inner potential value can be compensated for by an incorrect value of the coordination number. These results make clear that the 4+2 model for both oxides is *an artifact* of the EXAFS data analysis.

Valence Bond Analysis. It has been demonstrated recently by Hunter et al.[19] that in tetragonal zirconias the length of the longer bond is determined by the requirement that the sum of all valences constant:

$$\upsilon = \sum_j \exp^{((1.968-R_j)/0.326)}$$

where R_j is the length of the jth bond. Using the model as put foreward in this study with two subshells composed of four oxygens at 2.11 Å and four oxygens at 2.36 Å, a value for the valence of 3.92 is found close to the value of 3.96 as determined by Hunter et al.[20] If we consider now the 4+2 model as assumed by Vlaic et al.[2] a value of 3.29 is obtained. Even when a third shell with an additional two oxygens atoms located at a distance ≥ 2.6 Å were included, a valence ν smaller or equal than 3.45 was obtained. Therefore, in the 4+2 model, the ν (total valence) is far from 3.96, which also invalidates from a chemical point of view the 4+2 model.

Anharmonicity in the $Zr-O_2$ Pair Distribution Function. Using EXAFS data-analysis method I, a decrease of the coordination distance of the second Zr−O subshell was observed. In method III, by using the same phase and backscattering amplitude in the analysis of both subshells, a similar trend was observed. Furthermore, for the latter method a higher ΔE_0 value and a considerably higher Debye−Waller factor was observed for the second shell. High disorder associated with a large anharmonicity of the pair distribution function of a coordination shell can induce both an important underestimation of the distance and the coordination number if the normal EXAFS formalism[21] is used in the analysis. The normal EXAFS formalism is based upon a Gaussian type of disorder. The error in the distance introduces a large phase correction leading to high ΔE_0 values.

Application of the cumulant expansion approach (see Table 4) to analyze the EXAFS signal of the $Zr-O_2$ subshell led to the same coordination distances as found with XRD and an inner potential value close to the value found for the $Zr-O_1$ subshell (see Table 3). From these results it can be concluded that the $Zr-O_2$ subshell in the $Y_2O_3-ZrO_2$ standard sample and in $Ce_{0.5}Zr_{0.5}O_2$ must have an asymmetric pair distribution function. This also shows the same type of geometry in the two Zr−O subshells of the standard $Y_2O_3-ZrO_2$ and the $Ce_{0.5}Zr_{0.5}O_2$ sample.

It should be noticed that differences in distances are observed for the $Ce_{0.5}Zr_{0.5}O_2$ between the distance for the first shell defined by EXAFS and XRD owning to the atomic selectivity of EXAFS. In fact, in contrast to the Zr K edge EXAFS which allow the investigation of the oxygen shell selectively around the Zr, the XRD technique, due to the fact that Ce and Zr share the same atomic position, gives an averaged distance of the $Ce-O_1$ and the $Zr-O_1$ distances. Therefore, as Zr^{4+} (0.80 Å) present a smaller ionic radius compared to Ce^{4+}(0.97 Å), the distance Zr−O is overestimated by XRD technique as it is the case in fully stabilized cubic zirconia with oversized dopant cations as Gd.[22] However, as the composition of Y in the 1 mol % $Y-ZrO_2$ is very small, the Zr−O given by XRD are accurately describing the local structure around Zr and they are equal to those obtained by EXAFS analysis.

Structural Model: Explanation for Enhanced Oxygen Storage Capacity. Table 4 shows that the third cumulant (C_3) of the second Zr−O subshell in $Ce_{0.5}Zr_{0.5}O_2$ has a larger value than for the standard $Y_2O_3-ZrO_2$ sample. This means that the anharmonicity depends on the composition of the doped ZrO_2 oxides. The higher disorder associated with the second Zr−O subshell can be explained by the weakness of the chemical bond between the Zr and the oxygen atoms of the second shell. This

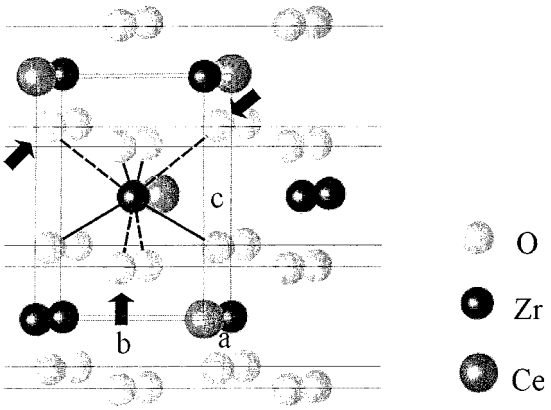

Figure 7. Schematic representation of the structure of the tetragonal $Ce_{0.5}Zr_{0.5}O_2$. The plain bold lines represent an oxygen tetrahedron associated with the $Zr-O_1$ *intra*layer bonds. The dotted bold lines are associated with the $Zr-O_2$ *inter*layer bonds. The dashed lines delimit the quadratic crystallographic cell. The thin horizontal plain lines define the layers of the lamellar structure. The α oxygen are pointed by arrows: they correspond to oxygen atom located in the second shell of a Zr atom also bounded to Ce in the same *intra*layer.

was proven by total energy calculations relying on the functional density theory.[23] In fact, the structure of tetragonal Y or Ce doped ZrO_2 can be considered as lamellar (see Figure 7). It is formed by oxygen tetrahedra layers with Zr atoms in their center.[7] The short $Zr-O_1$ distance corresponds to the *intra*layer Zr−O bond and the long $Zr-O_2$ distance to the *inter*layer Zr−O interaction. This also explains why the bonding between the Zr and the atoms of the second oxygen shell[7] is much weaker and possesses an asymmetric pair distribution function. The oxygen atom located in the second oxygen shell around Zr, which is also positioned in the second oxygen shell of a neighboring Y or Ce in the same *intra*layer will have an even weaker bond and will experience more asymmetry in the pair distribution function.

In automotive three way catalysts (TWCs) $Zr_xCe_{1-x}O_2$ mixed oxides present an enhancement of the oxygen storage/release capacity (OSC) compared to pure Ce oxide.[24] It is now possible to explain the origin of the enhancement of the redox properties.[24] The lamellar character of the structure the $Ce_{0.5}Zr_{0.5}O_2$ mixed oxide induces an enhancement of the oxygen diffusion in the material. Furthermore, the metal oxygen bond is particularly weak for the second oxygen subshell and thus very labile. The oxygen atoms of the second shell which are shared with a cerium atom, the α-oxygens as indicated in Figure 7, can then easily be removed from the structure during the Ce reduction process. The results obtained in this study lead to an understanding of the mechanism, which determines the OSC capacity in Ce oxide by doping with Zr.

Conclusion

Comparison of XRD, Zr K XANES, and EXAFS analysis data of a standard 1 mol % $Y_2O_3-ZrO_2$ with those obtained on a $Ce_{0.5}Zr_{0.5}O_2$ shows that both samples have a tetragonal structure with two shells of four oxygen atoms each around the Zr atom. EXAFS analysis assuming a Gaussian distribution function leads for both samples to a coordination distance in the $Zr-O_2$ subshell which is shorter than the value obtained with XRD. A large disorder associated with the second oxygen shell is detected. Because of this large disorder the classical EXAFS formalism leads to a wrong structural model. The use of a three-cumulant expansion in the EXAFS analysis describing an anharmonic pair distribution function resulted in the same coordination distances as found with XRD analysis.

The asymmetry parameter of the anharmonic pair distribution function in the $Zr-O_2$ subshell found in $Ce_{0.5}Zr_{0.5}O_2$ is larger than for the standard $Y_2O_3-ZrO_2$ sample. In the lamellar structure of the tetragonal Ce doped ZrO_2 the $Zr-O_2$ coordination forming the *inter*layer Zr−O interaction is much weaker than in the Y doped ZrO_2. This explains why the more labile $Zr-O_2$ bond enhances the OSC properties of $Ce_{0.5}Zr_{0.5}O_2$. The results of the present study show that the OSC properties in these oxides are determined by the asymmetry of the pair distribution function of the *inter*layer $Zr-O_2$ subshell.

Acknowledgment. The CEZIRENCAT network is supported by the European Union Training and Mobility of Researchers. WWW: http://www.dsch.univ.trieste.it/cezirencProgram. The authors thank the scientific staff of beamline BM29 of the ESRF (Grenoble, France).

References and Notes

(1) Kašpar, J.; Fornasiero, P.; Graziani, M. *Catal. Today* **1999**, *50*, 285.
(2) Vlaic, G.; Fornasiero, P.; Geremia, S.; Kaspar, J.; Graziani, M. *J. Catal.* **1997**, *168*, 386.
(3) Vlaic, G.; Di Monte, R.; Fornasiero, P.; Fonda, E.; Kaspar, J.; Graziani, M. *J. Catal.* **1999**, *182*, 378.
(4) Thuilier, M. H.; Dexpert-Ghys, J.; Dexpert, H.; Lagarde, P. *J. Solid State Chem.* **1987**, *69*, 153.
(5) Thromat, N.; Noguera, C.; Gautier, M.; Jollet, F.; Duraud, J. P. *Phys. Rev. B.* **1991**, *44*, 7904.
(6) Esquivias, L.; Barrera-Solano, C.; Pinero, M.; Prieto, C. *J. Alloys Compd.* **1996**, *239*, 71.
(7) Li, P.; Chen, I. W.; Penner-Hahn, J. E. *Phys. Rev. B.* **1993**, *48*, 10063.
(8) Yashima, M.; Arashi, H.; Kakihana, M.; Yoshimura, M. *J. Am. Ceram. Soc.* **1994**, *77*, 1067.
(9) Yashima, M.; Ishizawa, N.; Yoshimura, M. *J. Am. Ceram. Soc.* **1992**, *6*, 1541.
(10) Yashima, M.; Arashi, H.; Kakihana, M.; Yoshimura, M. *J. Am. Ceram. Soc.* **1994**, *77*, 1067.
(11) Golon, G.; Pijolat, M.; Valdivieso, F.; Vidal, H.; Kaspar, J.; Finnochio, E.; Daturi, M.; Binet, C.; Lavalley, J. C.; Baker, R. T.; Bernal, S. *J. Chem. Soc., Faraday Trans.* **1998**, *94*, 3717.
(12) Larson, A. L.; von Dreele, R. B. GSAS, LANSCE MS-H805; Los Alamos National Laboratory: Los Alamos, NM, 1985−1994.
(13) http://www.xs4all.nl/~xsi/.
(14) Vaarkamp, M.; Dring, I.; Oldman, R. J.; Stern, E. A.; Koningsberger, D. C. *Phys. Rev. B* **1994**, *50*, 7872.
(15) van Dorssen, G. E. Ph.D. Thesis, Utrecht University, The Netherlands, **1999**.
(16) Koninsberger, D. C.; Mojet, B. L.; van Dorssen, G. E.; Ramaker, D. E. *Top. Catal.* **2000**, *10*, 143.
(17) Argyriou, D. N.; Howard, C. J. *J. Appl. Crystallogr.* **1995**, *28*, 206.
(18) Eisenberger, P.; Brown, G. S. *Solid State Commun.* **1979**, *29*, 481.
(19) Crozier, E. D.; Rehr, J. J.; Ingalls, R. In *X-ray Absorption*, Koningsberger, D. C., Prins, R., Eds.; Wiley: New York, 1998.
(20) Li, P.; Chen, I.-W.; Penner-Hahn, J. E. *J. Am. Ceram. Soc.* **1994**, *77*, 118.
(21) Hunter, B. A.; Howard, C. J.; Kim, D.-J. M. J. *Solid State Chem.* **1999**, *146*, 363.
(22) Zamar, F.; Trovarelli, A.; de Leitenburg, C.; Dolcetti, C. *J. Chem. Soc., Chem. Commun. 965*, 1995.
(23) Tschope, A.; Liu, W.; Flytzanistephanopoulos, M.; Ying, J. Y. *J. Catal.* **1995**, *157*, 42.
(24) Fornasiero, P.; Balduci, G.; Di Monte, R.; Kašpar, J.; Sergo, V.; Gubitosa, G.; Ferrero, A.; Graziani, M. *J. Catal.* **1996**, *164*, 13.